ACS APPLIED MATERIALS & INTERFACES

Research Article

www.acsami.org

Lithium–Boron (Li–B) Monolayers: First-Principles Cluster Expansion and Possible Two-Dimensional Superconductivity

Chao Wu,[†] Hua Wang,[†] Jiajia Zhang,[‡] Gaoyang Gou,*[,†] Bicai Pan,[‡] and Ju Li*[,†,¶]

[†]Frontier Institute of Science and Technology, and State Key Laboratory for Mechanical Behavior of Materials, Xi'an Jiaotong University, Xi'an 710049, People's Republic of China

[‡]Department of Physics, University of Science and Technology of China, Hefei, Anhui 230026, People's Republic of China

[¶]Department of Nuclear Science and Engineering and Department of Materials Science and Engineering, Massachusetts Institute of Technology, Cambridge, Massachusetts 02139, United States

Supporting Information

ABSTRACT: Recent works demonstrated that the superconductivity at two-dimensional (2-D) can be achieved in Li-decorated graphene (*Nature Phys.* 2012, **8**, 131 and *Proc. Natl. Acad. Sci.* 2015, **112**, 11795). Inspired by the progress made in graphene, we predict by using the first-principles calculations that Li-incorporated B monolayers (Li–B monolayers) can be alternative 2-D superconductors. First-principles cluster expansion approach was used to evaluate the structural diversity and energetic stability of the 2-D Li–B monolayers by treating them as ternary $Li_x\hexagon_yB_{1-x-y}$ pseudoalloys ($\hexagon$ refers to B hexagonal hole). After thoroughly exploring the Li–B configuration space, several well-ordered and stable Li–B monolayers were identified. Detailed analyses regarding the electronic structures and lattice dynamics properties of the predicted Li–B monolayers were performed. Compared with the non-superconducting pure B-sheet, some predicted Li–B monolayers can exhibit the phonon-mediated superconducting properties above the liquid helium temperature.

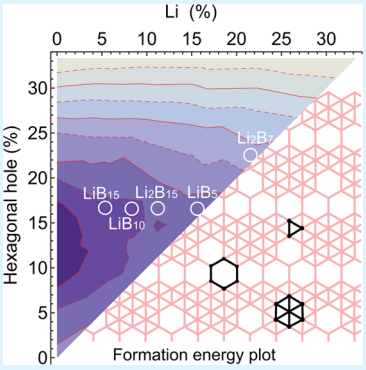

KEYWORDS: *two-dimensional materials, boron monolayers, phonon-mediated superconductivity, first-principles calculations, cluster-expansion approach*

1. INTRODUCTION

Superconductors composed of a single atomic monolayer are promising two-dimensional (2-D) components for nanoscale superconducting transistors and 2-D superconducting quantum interference devices.[1,2] In recent years, design and fabrication of 2-D superconductors have attracted increasing research efforts. Monolayer graphene and its derivatives have been widely investigated for such purpose. Although graphene itself is not an intrinsic superconductor, superconductivity can be induced in graphene sheet through adsorption of certain alkali metals.[3,4] Recent high-resolution angle-resolved photoemission spectroscopy measurement demonstrated that the superconducting temperature (T_C) of ~5.9 K can be realized in Li-decorated graphene.[5] As a result, Li-graphene monolayer can be an ideal platform for studying 2-D superconductivity. However, besides graphene and its derivatives, 2-D superconductivity is rarely reported in other planar monolayer systems. To enable an efficient and practical applications of 2-D superconductivity, more planar superconducting monolayer systems need to be developed.

Similar to carbon, the neighboring boron element also exhibits rich low-dimensional structures, including fullerene-type cage,[6−8] planar clusters,[9−12] one-dimensional nanotubes or nanowires,[13−15] and 2-D layers.[16−18] In particular, planar B-monolayers have honeycomb-like 2-D structures. On the basis of theoretical predictions, stable B-monolayers can be obtained by removing B atoms from a close-packed triangular B monolayer (denoted as B-$\triangle$), forming a binary $\hexagon_xB_{1-x}$ ($\hexagon$ stands for the hexagonal holes) pseudoalloy.[16,17] B-monolayers are predicted to have a rich structural diversity, as various B layered structures with different hexagonal hole concentrations ($x \cong 0.1-0.15$) and configurations are almost degenerate in energy.[17] Moreover, because of the delocalized nature of the π-derived bands, B-monolayers have metallic electronic properties similar to graphene.[16,19] Given the structural and electronic similarities between graphene and B-monolayers, it would be of fundamental interest to see whether 2-D superconductivity found in Li-decorated graphene could carry over to Li-incorporated B-monolayers as well.

In fact, boron can alloy with various alkali-metal or alkali-earth metals, forming the metal–boride compounds with different crystal structures and novel physical properties.[20,21] Especially, the metal–boride superconductor MgB_2 has an unexpected high transition temperature (T_C) of 39 K.[22,23] In a manner analogous to Li-decorated graphene, after introducing Li atoms into B-monolayers, planar Li–B layered structures

Received: October 19, 2015
Accepted: January 6, 2016
Published: January 6, 2016

DOI: 10.1021/acsami.5b09949
ACS Appl. Mater. Interfaces 2016, 8, 2526−2532

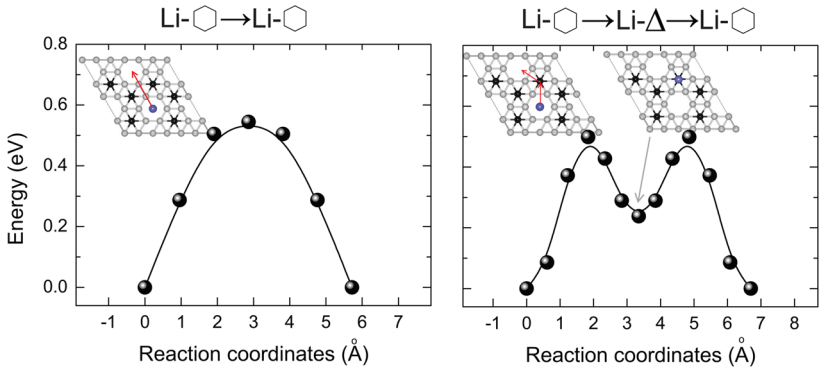

Figure 1. Energies and structures of Li adsorbed on a single-layer B-α sheet. Two minimum-energy paths for diffusion of a single Li atom between two adjacent B hexagonal hole sites (B-⬡), that is, across a B−B bond and triangular B (B-△), are simulated. The reaction coordinates are defined as the distance for the Li atom moving away from its initial state. Li and B atoms in the middle of the hexagons are represented as blue and black balls, respectively; other B atoms are in gray colors. Li-⬡ refers to the occupation of an empty B-hexagon by a single Li atom, while in Li-△ structure, Li atom is located over a B-filled hexagon.

may be formed. Considering the structural complexity of B-monolayers, Li−B monolayers may have even more complicated structural features. In this case, how to make a thorough exploration of planar Li−B configuration space and predict the stable Li−B layered structures? What are the atomic structures of the predicted Li−B monolayers? In the end, will the Li−B monolayers exhibit 2-D superconductivity as observed in Li-decorated graphene systems?[3−5]

To address the questions above, in the present work, we performed theoretical studies on Li-incorporated B-monolayers. First-principles based cluster-expansion method was used to explore the planar Li−B configuration space. Such a method has been successfully applied to many 2-D layered systems.[17,24−26] After evaluating the structural diversity and energetic stability of the planar Li−B structures, several stable and well-ordered Li−B monolayers were identified. Using the predicted Li−B layered structures, the detailed physical properties of Li−B monolayers were studied.

2. COMPUTATIONAL METHODS

Our density-functional theory (DFT) calculations are performed using two DFT implementations, namely, the Vienna ab initio Simulation Package (VASP)[27,28] and the Quantum Espresso code (QE).[29] Both DFT codes adopt the local spin-density approximation (LSDA)[30] as the exchange-correlation functional, unless otherwise stated. All Li−B monolayers are represented as slabs (shown in Figure 2) with a 15 Å vacuum region in the normal direction. Monkhorst−Pack k-point grid[31] of ∼40.8 k-points/Å^{-1} spacing is used to sample the reciprocal lattice of Li−B monolayer. In all calculations, atomic positions and lattice parameters in the lateral directions for Li−B monolayers are fully optimized until the residual Hellmann−Feynman forces are smaller than 0.01 eV/Å and the stresses less than 0.1 kbar.

VASP details: An energy cutoff of 450 eV and a plane-wave basis set within the projector augmented wave (PAW)[32] method are used. Diffusion of Li atom on B layer is evaluated by simulating the minimum energy path (MEP) trajectory using the nudged elastic band (NEB) method.[33,34] Electronic structures for the stable Li−B monolayers are further examined using the HSE hybrid functional.[35,36]

QE details: Nonlocal optimized norm-conserving pseudopotentials[37,38] and a plane-wave energy cutoff of 50 Ry are used for plane-wave calculations within QE. Phonon frequencies and electron−phonon coupling parameters are calculated based on density functional perturbation theory (DFPT).[39,40] Dense k-point and phonon-momentum q-point grid are used to obtain the converged phonon frequencies and electron−phonon coupling parameters during DFPT calculations.

3. RESULTS AND DISCUSSION

3.1. Cluster Expansion Model and Phase Stability.

Interaction between Li Atoms and B Monolayer. To predict the stable Li−B layered structures, the interactions between Li atoms and a single-layer B structure, namely, the B-α sheet,[16] are evaluated first. As shown in Figure 1, a Li atom adsorbs preferentially ($E_{binding}$ = −2.07 eV) at a B hexagonal hole site (B-⬡) of the B-α sheet, forming a stable Li-⬡ local structure. It is noted that $E_{binding}$ between the Li atom and the B-α sheet is even stronger than the cohesive energy of bulk Li (E_{coh} = −1.61 eV based on our calculation), indicating that Li atoms can adsorb uniformly on a B monolayer, rather than forming Li$_n$ clusters.[41,42] After the adsorption, the B-α sheet remains almost flat, and the distance between the Li atom and the B-α sheet is 1.67 Å. Bader charge analysis indicates that the Li atom transfers ∼0.5 electron to the B-α sheet; therefore, Li atoms act as *electron donors* to B layers.[43]

Li diffusional mobility on B-α sheet is studied by simulating the MEP of Li migration between the stable adsorption sites. Figure 1 illustrates our calculated migration pathways and the energy profiles along the MEP. Two pathways, separated by almost the same energy barrier (∼0.5 eV), correspond to a Li atom migrating across a B−B bond and triangular B site (B-△), respectively. It is clearly shown that a metastable state is formed when Li is adsorbed at a B-△ site, as such a Li-△ state will transform into a more stable Li-⬡ by overcoming a small barrier (∼0.25 eV). Therefore, Li-⬡, rather than Li-△, should be included as the structural component for constructing 2-D Li−B monolayers.

Model Li−B Monolayers Using Cluster Expansion Formalism. Similar to B-monolayers, whose structures are composed of B-△ and B-⬡ components,[16,17] Li−B monolayers can also be constructed by combining Li-⬡, B-⬡, and B-△, forming the ternary pseudoalloy $Li_x⬡_yB_{1-x-y}$. First-principles based cluster expansion (CE) method[44,45] can be applied to systematically study structural diversity and energetic stability of Li−B systems. The constructed Li−B monolayers contain two sublattices: honeycomb and triangular sublattices. As shown in Figure 2, the honeycomb sublattice is fully occupied by B atoms, while triangular sublattice site (hexagon center) can be either occupied by a vacancy or by a B or Li atom. Therefore, any Li−B configuration can be unambiguously expressed by a site occupancy vector $\vec{\sigma}$= {σ_1, σ_2, ...}, recording

DOI: 10.1021/acsami.5b09949
ACS Appl. Mater. Interfaces 2016, 8, 2526−2532

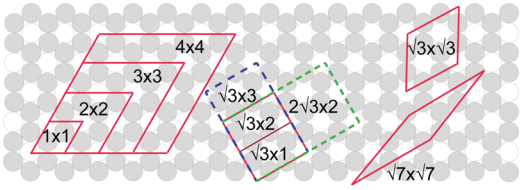

Figure 2. Supercells for simulating of Li−B monolayers. Honeycomb (●) and triangular sublattice (○) sites. For each supercell, various configurations with different arrangement of Li, B, and vacancy at triangular sublattice sites are considered. The smallest 1 × 1 supercell contains two honeycomb and one triangular sublattice sites.

the status of each site as a vacancy, a B atom, or a Li atom with the occupancy variable (σ_i = 0, 1, 2).[46]

Within the CE formalism, the energy of a given Li−B configuration ($\vec{\sigma}$) can be expressed as the energy contribution from the multicomponent cluster figures:

$$E(\vec{\sigma}) = J_0 + \sum_i J_i\sigma_i + \sum_{j<i} J_{i,j}\sigma_i\sigma_j + \sum_{k<j<i} J_{i,j,k}\sigma_i\sigma_j\sigma_k + \ldots \quad (1)$$

The indices i, j, and k run over all triangular sublattice sites. The expansion coefficients J refer to the effective cluster interactions (ECI), which give the energy contribution of each cluster figure. Alloy theoretical automated toolkit (ATAT)[47,48] is used to determine J, by fitting these coefficients to the calculated DFT energies of Li−B configurations. The cross-validation (CV) score,[47] which measures the configuration energy difference between the first-principles calculations and the CE predictions, is used to estimate the quality of the CE model. Iterative minimization of CV can finally lead to a set of good quality ECIs.

To make a thorough exploration of Li−B configuration space, various Li−B supercells (shown in Figure 2) are generated. In the present work, 10 types of supercells, with the largest one containing 48 lattice sites, and totally 197 symmetry-inequivalent configurations are calculated by DFT (tabulated in Supporting Information). Using the calculated DFT results, the CE with a small CV score (26.7 meV/lattice site) is achieved, and the corresponding ECI coefficients J are obtained. Our CE model contains 29 parameters (figures) up to five-body interaction terms. Inclusion of a larger number of parameters highlights the complexity of the ternary Li−B system. Except for the one-body figures (J = −1.741 and −0.203 eV for Li and B, respectively), most of the other terms are repulsive in nature, which are expected to produce ordered structures.[26]

Figure 3 summarizes the magnitude of J's and the corresponding figure geometries. The two-body figures have the dominating repulsive interactions, which naturally decrease with the pair distance. Specifically, the strength of J featuring B−B pairwise interactions (e.g., Figure 5 and 8) are significantly larger than those from Li−Li or Li−B pairs (Figures 4, 6, and 7). Therefore, B−B repulsive interactions primarily determine the structural features of Li−B monolayer. The repulsive interactions between B−B, Li−Li, and Li−B pairs are commonly known as surface coverage effects, as a result of the competitions among surface adsorbates.[46] These repulsive interactions are eventually in balance with the attractions from the one-body figures, leading to the limited adsorbate (Li-⬡ and B-△) concentration in stable Li−B monolayers. Compared with two-body terms, four-body and five-body

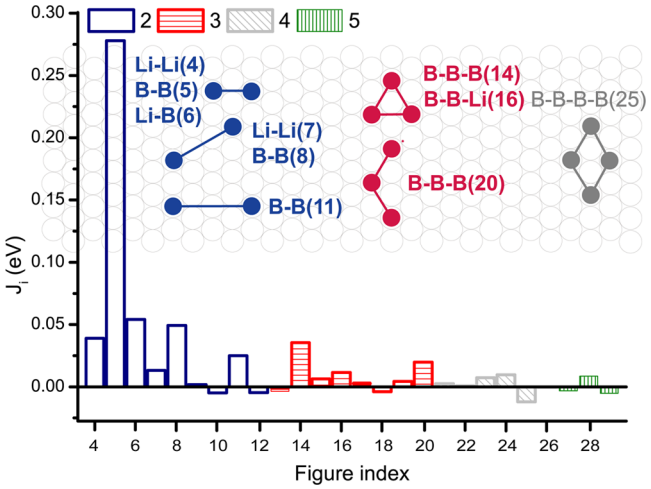

Figure 3. Effective cluster interaction (excluding the empty and one-body figures) J for Li−B configurations. Figures corresponding to 10 leading ECI are shown as the ball-and-stick models. Two, three, and four-body clusters are marked in blue, red, and gray colors, respectively.

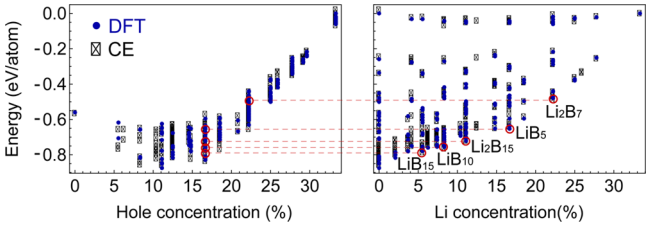

Figure 4. Formation energies for 371 symmetry-inequivalent Li−B configurations calculated from CE and 197 configurations obtained from first-principles calculations, with respect to hexagonal hole and Li concentrations. Hexagonal hole concentration is defined as (No. of B-⬡ + Li-⬡)/(No. of triangular sublattice sites).

figures are characterized by the interactions with small intensities. However, considering the large number of their multiplicity, these many-body figures are indispensable in reproducing DFT configuration energy.

The configuration energy of any symmetry-inequivalent Li−B structure (371 in total) can now be calculated using the constructed CE model. Formation energy e_f is then used to evaluate the energetic stability of Li−B configuration, which is defined as

$$e_f = \frac{E_{conf} - N_{Li} \times \mu_{Li} - N_B \times \mu_B}{N_{Li} + N_B} \quad (2)$$

where μ_B and μ_{Li} refer to the atomic energy of the B-α sheet and an isolated Li atom, respectively. Figure 4 gives formation energy e_f of all Li−B configurations calculated using DFT and CE methods. There is a good agreement between DFT calculations and CE predictions, as CE well reproduces DFT ground-state results. As a ternary system, a Li−B configuration ($Li_x⬡_yB_{1-x-y}$) has two component variables. We first examine e_f of Li−B as a function of the hexagonal hole concentration ($\{x + y\}$%), the corresponding formation energy plot exhibits a convex hull ∼10−15%, where the stable *Li-free* B-monolayer structures ($⬡_xB_{1-x}$ configurations) are found. Such a finding is quite consistent with previous CE results on B-monolayers.[17] In the formation energy versus Li concentration ($\{x\}$%) plot, there exist several well-ordered and stable Li−B configurations

DOI: 10.1021/acsami.5b09949
ACS Appl. Mater. Interfaces 2016, 8, 2526−2532

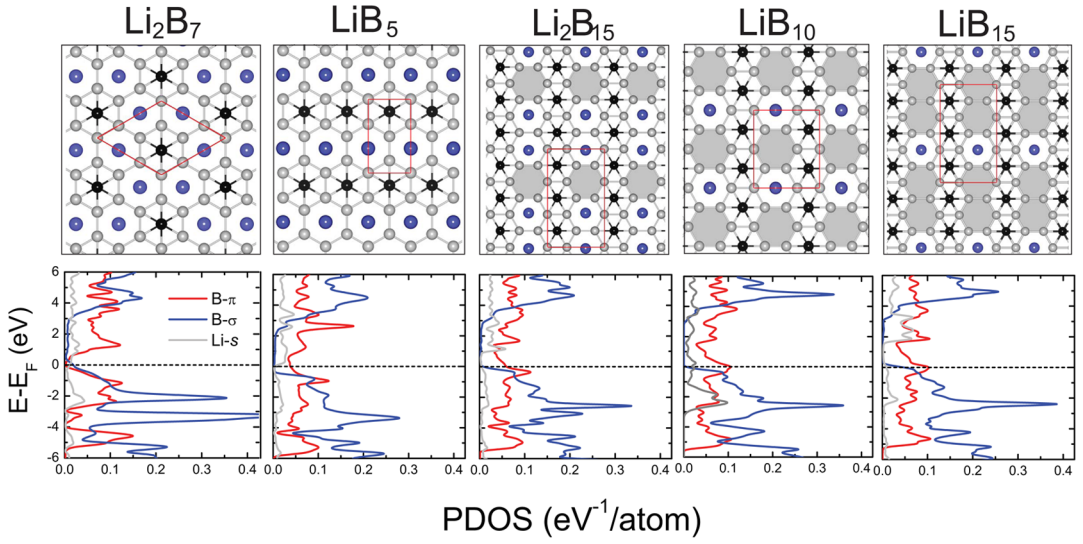

Figure 5. Crystal structures and projected density of states (PDOS) for the stable 2D Li−B monolayers obtained from CE simulations. The blue and gray balls represent Li and B atoms located at the center of B-hexagons, while other B atoms are marked in gray colors. Primary unit cells are indicated by red lines. B-hexagonal holes (B-⬡) are marked as dark gray areas. In PDOS plots, B-σ are composed of planar B-s, p_x and p_y states. B-π is derived from B-p_z state.

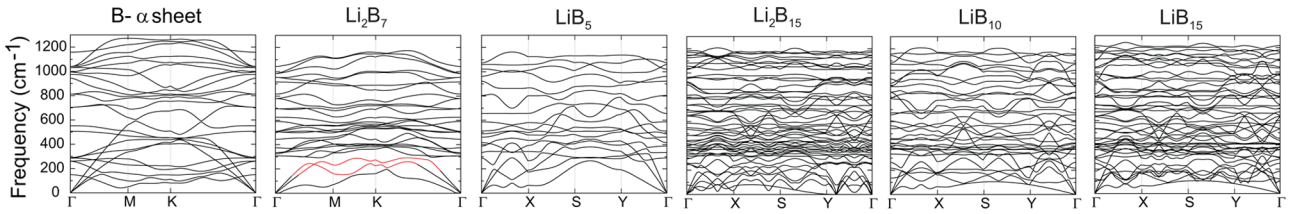

Figure 6. Phonon frequency dispersions for B-α sheet and Li−B monolayers. All predicted 2D Li−B structures are vibrationally stable. Compared with B-α sheet, the softened acoustic phonon branches ~200 cm^{-1} in Li_2B_7 are marked in red color.

with certain stoichiometry: Li_2B_7, LiB_5, Li_2B_{15}, LiB_{10}, and LiB_{15}. We will therefore focus on these CE-predicted Li−B layered structures and present the detailed property analyses in the following sections.

3.2. Properties of the Predicted Li−B Monolayers. *Electronic Properties.* The low-energy 2-D Li−B structures predicted using CE methods are shown in Figure 5. Li_2B_{15}, LiB_{10}, and LiB_{15} contain B-⬡, B-△, and Li-⬡ structural components, while Li_2B_7 and LiB_5 with high Li concentration are composed of Li-⬡ and B-△ only. Interestingly, LiB_{15} structure has two neighboring B-⬡ holes. Such a local structure was also detected in some experimental planar B-clusters.[10,12] For each Li−B monolayer, planar s + p_x + p_y orbitals from B atoms are hybridized to form the in-plane σ bonds, and the out-of-plane π bonds come from p_z orbitals. Orbital-resolved density of states for Li−B monolayers are analyzed and presented in Figure 5. All Li−B monolayers are metallic, as the delocalized p_z−π orbitals from B atoms are partially filled. Moreover, there is a large energy separation between bonding σ states and antibonding σ^* states, and Fermi energy level (E_F) of the system falls into the σ−σ^* gap. Therefore, all Li−B monolayers have the almost fully filled σ states and empty σ^* states.

The stabilities of our predicted Li−B structures can be explained from the nature of their electronic bonding.[16] Similar to the stable B monolayers,[17] Li−B monolayers also satisfy the optimal electron-filling principle: electrons optimally fill the in-plane bonding σ states, making bonding σ states fully filled and leaving antibonding σ^* states empty. Moreover, Li atoms stabilize the 2D Li−B monolayers by donating their electrons to the B network (~0.4 e per Li atom). Without Li doping, the corresponding B layers alone will be unstable, as the bonding σ states will be partially filled, and the Fermi energy level will be located within σ states of the system (Figure S1 of the Supporting Information).

Because of the deficiencies of LDA method in predicting the energy band gaps of the calculated system, a more accurate Heyd−Scuseria−Ernzerhof (HSE) hybrid exchange-correlation functional, which includes screened exact exchange interaction,[35,36] is employed to verify the metallicity of Li−B monolayers. After performing the HSE calculations for several systems, we find that the metallic features of Li−B monolayers are still retained at hybrid functional level (Figure S2 of the Supporting Information), except that the HSE-predicted energy peaks are slightly different from the LDA results. Therefore, metallic electronic states are intrinsic ground states for Li−B monolayers.

Lattice Dynamics and Superconducting Properties. To verify the dynamic stabilities of the predicted Li−B monolayers, we further examine their lattice dynamics properties using DFPT method implemented in QE. Converged phonon frequencies are obtained after using dense k-point and phonon-momentum q-point grids. For example, $\sqrt{3} \times \sqrt{3}$ supercell shown in Figure 2 is simulated using 18 × 18 × 1 k-grid and 4 × 4 × 1 q-grid, respectively. Shown in Figure 6 are our calculated phonon dispersions for Li−B monolayers along the high-symmetry directions in the Brillouin zone. Unstable phonon modes with imaginary frequencies are absent in the

DOI: 10.1021/acsami.5b09949
ACS Appl. Mater. Interfaces 2016, 8, 2526−2532

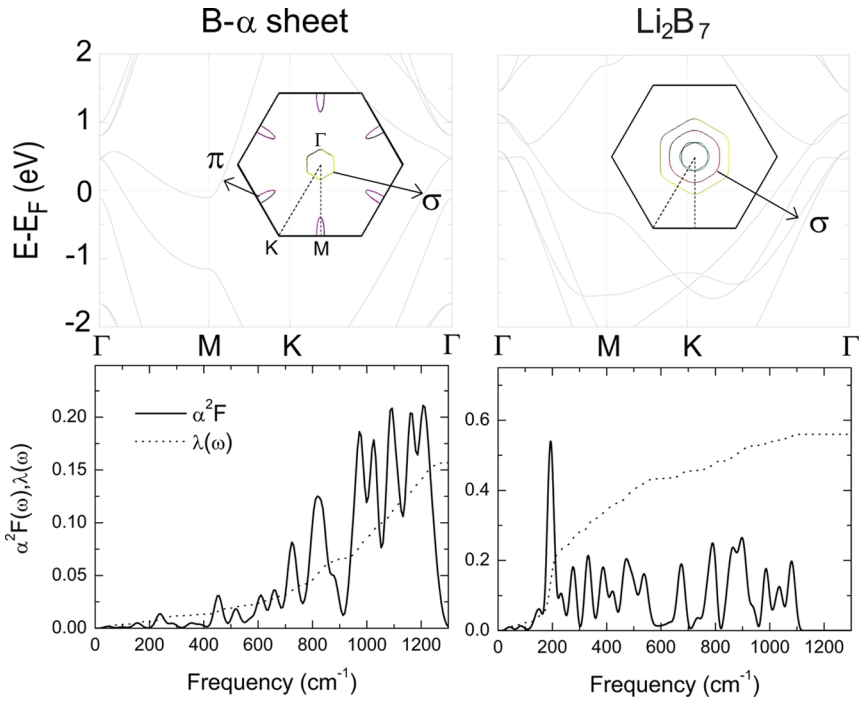

Figure 7. Comparison of electronic band-structures, Eliashberg spectral functions $\alpha^2F(\omega)$ and frequency-dependent EPC functions $\lambda(\omega)$ between B-α sheet and Li_2B_7 layer. (inset) Fermi surface plots of the two structures. σ and π bands appearing in Fermi surface plots are indicated by arrows.

entire Brillouin zones; therefore, our predicted Li−B monolayers are vibrationally stable and free of structural instabilities.

To quantify the electron−phonon coupling of Li−B monolayers, detailed analysis of the electronic structures of the system is required. We focus on two representative systems: B-α sheet and Li_2B_7, and compare their electronic structures in detail. Figure 7 shows our calculated band structures and Fermi surface plots. In the B-α sheet, two isolated σ and π bands cross the Fermi level, forming two types of Fermi surfaces: a small circle (σ band) centered at the Γ point and six open-pockets (π band) along the Γ-M directions. Since Li atoms act as electron donors to B layers, there are more electronic bands (σ only) crossing the Fermi level of Li_2B_7, leading to a significant increase of electron density around the Fermi level.

Phonon-mediated superconducting properties[49,50] of the B-α sheet and Li_2B_7 are further investigated by calculating the electron−phonon coupling (EPC) parameters and superconducting temperature T_C, using the McMillan−Allen−Dynes formula.[51,52] Figure 7 shows our calculated Eliashberg spectral function $\alpha^2F(\omega)$ ($\alpha^2F(\omega)$ gives the contribution of each phonon mode to the total EPC intensity) and frequency-dependent EPC functions $\lambda(\omega)$. Taking the Coulomb pseudopotential $\mu^* = 0.12$,[53] the superconducting temperature T_C can be obtained (computational details in Supporting Information). The B-α sheet has a small EPC constant of 0.16, which is mainly contributed by the high-frequency (600−1200 cm^{-1}) B−B stretching modes. On the basis of Bardeen−Cooper−Schrieffer (BCS) theory,[49,50] as the phonon-mediated attraction is not strong enough to overcome the Coulomb repulsion ($\lambda = 0.16$ vs $\mu^* = 0.12$), electron Cooper pairs cannot be formed. Therefore, B-α sheet is a non-superconducting metal (Table 1). In Li_2B_7, the Eliashberg spectral function $\alpha^2F(\omega)$ has a predominant peak around 200 cm^{-1}, corresponding to the coupling between the σ-band electrons and the softened in-plane acoustic modes (red phonon branches in Figure 6). Moreover, $\lambda(\omega)$ of Li_2B_7 are mainly contributed by low-frequency phonons below 600 cm^{-1}. This leads to a stronger EPC constant ($\lambda = 0.56$) and T_C of 6.2 K for Li_2B_7.

Table 1

	$N(E_F)$[a]	λ[b]	ω_{log}[c] (K)	ω_0[d] (cm^{-1})	T_C[e]
B-α	0.10	0.16	1141.19	939.8	
Li_2B_7	0.37	0.56	462.79	492.1	6.2

[a]Calculated electronic DOS at the Fermi level $N(E_F)$ (in states/atom). [b]Electron−phonon coupling (EPC) constant. [c]Logarithmic frequency average ω_{log}. [d]Characteristic phonon frequency ω_0 dominating the EPC. [e]Superconducting critical temperature T_C for the B-α sheet and Li_2B_7 layer. Retarded Coulomb pseudopotential $\mu^* = 0.12$ is used for calculations. The relation between λ, $N(E_F)$ and ω_0 can be expressed as $\lambda = V_{ep}\cdot N(E_F)$ and $\lambda \propto \omega_0^{-2}$.

The interplay between phonon frequencies, electron density of states, and superconducting properties of the system can be described by the following relation:[51,53]

$$\lambda = V_{ep}\cdot N(E_F)$$
$$\lambda \propto \frac{1}{\omega_0^2}, \quad \text{with } \omega_0 = \sqrt{\frac{\int d\omega \alpha^2F(\omega)\cdot\omega}{\int d\omega \alpha^2F(\omega)/\omega}} \qquad (3)$$

where V_{ep} is the mean electron−phonon pairing potential around the Fermi level. The characteristic phonon frequency ω_0 is defined as the average of all phonon frequencies weighted by the Eliashberg spectral function $\alpha^2F(\omega)$. Both B-α sheet and Li_2B_7 belong to $\sqrt{3}\times\sqrt{3}$ supercell (Figure 2), which can be characterized by the same V_{ep} ($V_{ep} = 1.51$ eV). Their calculated EPC constant λ is exactly linearly proportional to electron density of states $N(E_F)$ and inversely proportional to ω_0^2 (Table 1), matching eq 3 quite well.

For a phonon-mediated BCS superconductor, it requires a strong electron−phonon coupling to overcome the electron−

DOI: 10.1021/acsami.5b09949
ACS Appl. Mater. Interfaces 2016, 8, 2526−2532

electron repulsion interactions. On the basis of eq 3, the large electron density of states at Fermi level $N(E_F)$ and soft characteristic phonon frequency ω_0 are required to generate the strong EPC constant. In the case of B-α sheet, the limited electron density $N(E_F)$ and high-frequency ω_0 give rise to an overall weak electron−phonon coupling, making B-α sheet itself as non-superconducting metal. As a consequence of electron doping enabled by Li atoms, there are more σ bands crossing Fermi level in Li_2B_7, and the softened in-plane acoustic phonon modes are in strong coupling with the σ bands, which finally leads to a strong EPC constant. As Li_2B_7 has the highest Li concentration and consequently the largest electron density $N(E_F)$, Li_2B_7 exhibits the optimized superconducting properties among all predicted Li−B monolayers (Table SII). However, compared with MgB_2 whose EPC constant $\lambda > 1$,[54] the electron−phonon coupling in Li_2B_7 is much weaker. This is because only σ states contribute to λ in Li_2B_7, while both σ and π states have considerable contribution to the electron−phonon coupling in MgB_2.[23,54] But still, Li_2B_7 has superconducting temperature T_C above the liquid helium temperature, comparable with other 2-D superconductors, such as Li-decorated graphene ($T_C \cong 5.9$ K).[5] Therefore, our predicted Li−B monolayers offer great opportunities for investigating the superconducting properties of 2-D atomic sheets.

4. CONCLUSIONS

In summary, by combining the first-principles calculations and cluster expansion model, we have explored the configuration space of Li-incorporated B monolayers. Li−B monolayers resemble ternary $Li_x\bigcirc_yB_{1-x-y}$ pseudoalloy system, whose configuration space is computationally challenging to explore. Nevertheless, CE models are successfully applied to the planar Li−B configurations, providing good quality in reproducing DFT ground-state results. On the basis of the CE model, several well-ordered and low-energy Li−B monolayers are identified. We have addressed the physical origins regarding the energetic stability and lattice dynamics properties of the predicted Li−B monolayers. We further demonstrated that, after incorporation of Li atoms, Li−B monolayers can exhibit the phonon-mediated superconducting properties, which are absent in the planar B sheet. Especially superconducting temperature T_C of layered Li_2B_7 can exceed the liquid helium temperature.

■ ASSOCIATED CONTENT

Supporting Information

The Supporting Information is available free of charge on the ACS Publications website at DOI: 10.1021/acsami.5b09949.

The structural parameters for all Li−B supercells. Detailed electronic structure results for Li−B monolayers and computational details of the electron−phonon coupling calculations. (PDF)

■ AUTHOR INFORMATION

Corresponding Authors

*E-mail: gougaoyang@mail.xjtu.edu.cn. (G.G.)
*E-mail: liju@mit.edu. (J.L.)

Notes

The authors declare no competing financial interest.

■ ACKNOWLEDGMENTS

The authors acknowledge the funding support from National Basic Research Program of China, under Contract No. 2012CB619402, and National Science Foundation of China, under Contract Nos. 11204230, 11574244, and 21203143. J.L. acknowledges support by NSF DMR-1410636. National supercomputer center (NSCC) in Tianjin is acknowledged for computational support.

■ REFERENCES

(1) Delahaye, J.; Hassel, J.; Lindell, R.; Sillanpää, M.; Paalanen, M.; Seppä, H.; Hakonen, P. Low-Noise Current Amplifier Based on Mesoscopic Josephson Junction. *Science* **2003**, *299*, 1045−1048.

(2) De Franceschi, S.; Kouwenhoven, L.; Schönenberger, C.; Wernsdorfer, W. Hybrid Superconductor-Quantum Dot Devices. *Nat. Nanotechnol.* **2010**, *5*, 703−711.

(3) Profeta, G.; Calandra, M.; Mauri, F. Phonon-Mediated Superconductivity in Graphene by Lithium Deposition. *Nat. Phys.* **2012**, *8*, 131−134.

(4) Xue, M.; Chen, G.; Yang, H.; Zhu, Y.; Wang, D.; He, J.; Cao, T. Superconductivity in Potassium-Doped Few-Layer Graphene. *J. Am. Chem. Soc.* **2012**, *134*, 6536−6539.

(5) Ludbrook, B. M.; Levy, G.; Nigge, P.; Zonno, M.; Schneider, M.; Dvorak, D. J.; Veenstra, C. N.; Zhdanovich, S.; Wong, D.; Dosanjh, P.; Strasser, C.; Stoehr, A.; Forti, S.; Ast, C. R.; Starke, U.; Damascelli, A. Evidence for Superconductivity in Li-decorated Monolayer Graphene. *Proc. Natl. Acad. Sci. U. S. A.* **2015**, *112*, 11795−11799.

(6) Gonzalez Szwacki, N.; Sadrzadeh, A.; Yakobson, B. I. B_{80} fullerene: an *ab initio* Prediction of Geometry, Stability, and Electronic Structure. *Phys. Rev. Lett.* **2007**, *98*, 166804.

(7) Oger, E.; Crawford, N. R.; Kelting, R.; Weis, P.; Kappes, M. M.; Ahlrichs, R. Boron Cluster Cations: Transition from Planar to Cylindrical Structures. *Angew. Chem., Int. Ed.* **2007**, *46*, 8503−8506.

(8) Lv, J.; Wang, Y.; Zhu, L.; Ma, Y. B_{38}: an All-Boron Fullerene Analogue. *Nanoscale* **2014**, *6*, 11692.

(9) Li, W.-L.; Zhao, Y.-F.; Hu, H.-S.; Li, J.; Wang, L.-S. $[B_{30}]^-$: A Quasiplanar Chiral Boron Cluster. *Angew. Chem.* **2014**, *126*, 5646−5651.

(10) Li, W.-L.; Chen, Q.; Tian, W.-J.; Bai, H.; Zhao, Y.-F.; Hu, H.-S.; Li, J.; Zhai, H.-J.; Li, S.-D.; Wang, L.-S. The B_{35} Cluster with a Double-Hexagonal Vacancy: A New and More Flexible Structural Motif for Borophene. *J. Am. Chem. Soc.* **2014**, *136*, 12257−12260.

(11) Piazza, Z. A.; Hu, H.-S.; Li, W.-L.; Zhao, Y.-F.; Li, J.; Wang, L.-S. Planar Hexagonal B_{36} as a Potential Basis for Extended Single-Atom Layer Boron Sheets. *Nat. Commun.* **2014**, *5*, 3113.

(12) Zhai, H.-J.; Zhao, Y.-F.; Li, W.-L.; Chen, Q.; Bai, H.; Hu, H.-S.; Piazza, Z. A.; Tian, W.-J.; Lu, H.-G.; Wu, Y.-B.; Mu, Y.-W.; Wei, G.-F.; Liu, Z.-P.; Li, J.; Li, S.-D.; Wang, L.-S. Observation of an All-Boron Fullerene. *Nat. Chem.* **2014**, *6*, 727−731.

(13) Ciuparu, D.; Klie, R. F.; Zhu, Y.; Pfefferle, L. Synthesis of Pure Boron Single-Wall Nanotubes. *J. Phys. Chem. B* **2004**, *108*, 3967−3969.

(14) Xu, T. T.; Zheng, J.-G.; Wu, N.; Nicholls, A. W.; Roth, J. R.; Dikin, D. A.; Ruoff, R. S. Crystalline Boron Nanoribbons: Synthesis and Characterization. *Nano Lett.* **2004**, *4*, 963−968.

(15) Singh, A. K.; Sadrzadeh, A.; Yakobson, B. I. Probing Properties of Boron α-Tubes by ab initio Calculations. *Nano Lett.* **2008**, *8*, 1314−1317.

(16) Tang, H.; Ismail-Beigi, S. Novel Precursors for Boron Nanotubes: the Competition of Two-Center and Three-Center Bonding in Boron Sheets. *Phys. Rev. Lett.* **2007**, *99*, 115501.

(17) Penev, E. S.; Bhowmick, S.; Sadrzadeh, A.; Yakobson, B. I. Polymorphism of Two-Dimensional Boron. *Nano Lett.* **2012**, *12*, 2441−2445.

(18) Wu, X.; Dai, J.; Zhao, Y.; Zhuo, Z.; Yang, J.; Zeng, X. C. Two-Dimensional Boron Monolayer Sheets. *ACS Nano* **2012**, *6*, 7443−7453.

(19) Yang, X.; Ding, Y.; Ni, J. *Ab initio* Prediction of Stable Boron Sheets and Boron Nanotubes: Structure, Stability, and Electronic

DOI: 10.1021/acsami.5b09949
ACS Appl. Mater. Interfaces 2016, 8, 2526−2532

Properties. *Phys. Rev. B: Condens. Matter Mater. Phys.* **2008**, *77*, 041402.
(20) Hermann, A.; McSorley, A.; Ashcroft, N. W.; Hoffmann, R. From Wade-Mingos to Zintl-Klemm at 100 GPa: Binary Compounds of Boron and Lithium. *J. Am. Chem. Soc.* **2012**, *134*, 18606−18618.
(21) Peng, F.; Miao, M.; Wang, H.; Li, Q.; Ma, Y. Predicted Lithium-Boron Compounds under High Pressure. *J. Am. Chem. Soc.* **2012**, *134*, 18599−18605.
(22) Nagamatsu, J.; Nakagawa, N.; Muranaka, T.; Zenitani, Y.; Akimitsu, J. Superconductivity at 39 K in Magnesium Diboride. *Nature* **2001**, *410*, 63−64.
(23) Choi, H. J.; Roundy, D.; Sun, H.; Cohen, M. L.; Louie, S. G. The Origin of the Anomalous Superconducting Properties of MgB_2. *Nature* **2002**, *418*, 758−760.
(24) Luo, X.; Yang, J.; Liu, H.; Wu, X.; Wang, Y.; Ma, Y.; Wei, S.-H.; Gong, X.; Xiang, H. Predicting Two-Dimensional Boron-Carbon Compounds by the Global Optimization Method. *J. Am. Chem. Soc.* **2011**, *133*, 16285−16290.
(25) Lee, E.; Persson, K. A. Li Absorption and Intercalation in Single Layer Graphene and Few Layer Graphene by First Principles. *Nano Lett.* **2012**, *12*, 4624−4628.
(26) Huang, B.; Xiang, H.; Xu, Q.; Wei, S.-H. Overcoming the Phase Inhomogeneity in Chemically Functionalized Graphene: the Case of Graphene Oxides. *Phys. Rev. Lett.* **2013**, *110*, 085501.
(27) Kresse, G.; Furthmüller, J. Efficient Iterative Schemes for *ab initio* Total-Energy Calculations using a Plane-Wave Basis Set. *Phys. Rev. B: Condens. Matter Mater. Phys.* **1996**, *54*, 11169−11186.
(28) Kresse, G.; Joubert, D. From Ultrasoft Pseudopotentials to the Projector Augmented-Wave Method. *Phys. Rev. B: Condens. Matter Mater. Phys.* **1999**, *59*, 1758−1775.
(29) Giannozzi, P.; Baroni, S.; Bonini, N.; Calandra, M.; Car, R.; Cavazzoni, C.; Ceresoli, D.; Chiarotti, G. L.; Cococcioni, M.; Dabo, I.; dal Corso, A.; de Gironcoli, S.; Fabris, S.; Fratesi, G.; Gebauer, R.; Gerstmann, U.; Gougoussis, C.; Kokalj, A.; Lazzeri, M.; Martin-Samos, L.; Marzari, N.; Mauri, F.; Mazzarello, R.; Paolini, S.; Pasquarello, A.; Paulatto, L.; Sbraccia, C.; Scandolo, S.; Sclauzero, G.; Seitsonen, A. P.; Smogunov, A.; Umari, P.; Wentzcovitch, R. M. QUANTUM ESPRESSO: a Modular and Open-Source Software Project for Quantum Simulations of Materials. *J. Phys.: Condens. Matter* **2009**, *21*, 395502.
(30) Perdew, J. P.; Zunger, A. Self-Interaction Correction to Density-Functional Approximations for Many-Electron Systems. *Phys. Rev. B: Condens. Matter Mater. Phys.* **1981**, *23*, 5048−5079.
(31) Monkhorst, H. J.; Pack, J. D. Special Points for Brillouin-Zone Integrations. *Phys. Rev. B* **1976**, *13*, 5188−5192.
(32) Blöchl, P. E. Projector Augmented-Wave Method. *Phys. Rev. B: Condens. Matter Mater. Phys.* **1994**, *50*, 17953−17979.
(33) Henkelman, G.; Uberuaga, B. P.; Jónsson, H. A Climbing Image Nudged Elastic Band Method for Finding Saddle Points and Minimum Energy Paths. *J. Chem. Phys.* **2000**, *113*, 9901−9904.
(34) Henkelman, G.; Jónsson, H. Improved Tangent Estimate in the Nudged Elastic Band Method for Finding Minimum Energy Paths and Saddle Points. *J. Chem. Phys.* **2000**, *113*, 9978−9985.
(35) Heyd, J.; Scuseria, G. E.; Ernzerhof, M. Hybrid Functionals based on A Screened Coulomb Potential. *J. Chem. Phys.* **2003**, *118*, 8207−8215.
(36) Heyd, J.; Scuseria, G. E.; Ernzerhof, M. Erratum: "Hybrid Functionals based on A Screened Coulomb Potential. *J. Chem. Phys.* **2006**, *124*, 219906−219906.
(37) Rappe, A. M.; Rabe, K. M.; Kaxiras, E.; Joannopoulos, J. D. Optimized Pseudopotentials. *Phys. Rev. B: Condens. Matter Mater. Phys.* **1990**, *41*, 1227−1230.
(38) Ramer, N. J.; Rappe, A. M. Designed Nonlocal Pseudopotentials for Enhanced Transferability. *Phys. Rev. B: Condens. Matter Mater. Phys.* **1999**, *59*, 12471−12478.
(39) Baroni, S.; de Gironcoli, S.; dal Corso, A. D.; Giannozzi, P. Phonons and Related Crystal Properties from Density-Functional Perturbation Theory. *Rev. Mod. Phys.* **2001**, *73*, 515−562.
(40) Gonze, X. Adiabatic Density-Functional Perturbation Theory. *Phys. Rev. A: At., Mol., Opt. Phys.* **1995**, *52*, 1096−1114.
(41) Yildirim, H.; Kinaci, A.; Zhao, Z.-J.; Chan, M. K. Y.; Greeley, J. P. First-Principles Analysis of Defect-Mediated Li Adsorption on Graphene. *ACS Appl. Mater. Interfaces* **2014**, *6*, 21141−21150.
(42) Zhou, J.; Sun, Q.; Wang, Q.; Jena, P. Tailoring Li Adsorption on Graphene. *Phys. Rev. B: Condens. Matter Mater. Phys.* **2014**, *90*, 205427.
(43) Zheng, B.; Yu, H.-T.; Xie, Y.; Lian, Y.-F. Engineering the Work Function of Buckled Boron *alpha*-Sheet by Lithium Adsorption: A First-Principles Investigation. *ACS Appl. Mater. Interfaces* **2014**, *6*, 19690−19701.
(44) Sanchez, J. M.; Ducastelle, F.; Gratias, D. Generalized Cluster Description of Multicomponent Systems. *Phys. A* **1984**, *128*, 334−350.
(45) Van de Walle, A.; Ceder, G. Automating First-Principles Phase Diagram Calculations. *J. Phase Equilib.* **2002**, *23*, 348−359.
(46) Wu, C.; Schmidt, D.; Wolverton, C.; Schneider, W. Accurate Coverage-Dependence Incorporated into First-Principles Kinetic Models: Catalytic NO Oxidation on Pt (111). *J. Catal.* **2012**, *286*, 88−94.
(47) Van de Walle, A.; Asta, M.; Ceder, G. The Alloy Theoretic Automated Toolkit: A User Guide. *CALPHAD: Comput. Coupling Phase Diagrams Thermochem.* **2002**, *26*, 539−553.
(48) Van de Walle, A. Multicomponent Multisublattice. Alloys, Nonconfigurational Entropy and Other Additions to the Alloy Theoretic Automated Toolkit. *CALPHAD: Comput. Coupling Phase Diagrams Thermochem.* **2009**, *33*, 266−278.
(49) Bardeen, J.; Cooper, L.; Schrieffer, J. Microscopic Theory of Superconductivity. *Phys. Rev.* **1957**, *106*, 162−164.
(50) Bardeen, J.; Cooper, L.; Schrieffer, J. Theory of Superconductivity. *Phys. Rev.* **1957**, *108*, 1175−1204.
(51) McMillan, W. Transition Temperature of Strong-Coupled Superconductors. *Phys. Rev.* **1968**, *167*, 331−344.
(52) Allen, P. B.; Dynes, R. C. Transition Temperature of Strong-Coupled Superconductors Reanalyzed. *Phys. Rev. B* **1975**, *12*, 905−922.
(53) Si, C.; Liu, Z.; Duan, W.; Liu, F. First-Principles Calculations on the Effect of Doping and Biaxial Tensile Strain on Electron-Phonon Coupling in Graphene. *Phys. Rev. Lett.* **2013**, *111*, 196802.
(54) Liu, A. Y.; Mazin, I.; Kortus, J. Beyond Eliashberg Superconductivity in MgB_2: Anharmonicity, Two-Phonon Scattering, and Multiple Gaps. *Phys. Rev. Lett.* **2001**, *87*, 087005.

DOI: 10.1021/acsami.5b09949
ACS Appl. Mater. Interfaces 2016, 8, 2526−2532